Inorganic Chemistry
Article
pubs.acs.org/IC

Anion Disorder in Lanthanoid Zirconates $Gd_{2-x}Tb_xZr_2O_7$

Emily Reynolds, Peter E. R. Blanchard, Brendan J. Kennedy,* Chris D. Ling, and Samuel Liu

School of Chemistry, The University of Sydney, Sydney, NSW 2006 Australia

Max Avdeev and Zhaoming Zhang

Australian Nuclear Science and Technology Organisation, Lucas Heights, New South Wales, 2234, Australia

Gabriel J. Cuello

Institut Laue-Langevin, BP 156, 6 rue Jules Horowitz, 38042 Grenoble Cedex 9, France

Anton Tadich

Australian Synchrotron, 800 Blackburn Road, Clayton, Victoria 3168, Australia

Ling-Yun Jang

Facility Utilization Group, Experiment Facility Division, National Synchrotron Radiation Research Center, Hsinchu 30076, Taiwan

Supporting Information

ABSTRACT: The pyrochlore−defect fluorite order−disorder transition has been studied for a series of oxides of the type $Gd_{2-x}Tb_xZr_2O_7$ by a combination of diffraction and spectroscopy techniques. Synchrotron X-ray diffraction data suggest an abrupt transition from the coexistence of pyrochlore and defect fluorite phases to a single defect fluorite phase with increasing Tb content. However neutron diffraction data, obtained at $\lambda \approx 0.497$ Å for all Gd-containing samples to minimize absorption, not only provide evidence for independent ordering of the anion and cation sublattices but also suggest that the disorder transition across the pyrochlore−defect fluorite boundary of $Ln_2Zr_2O_7$ is rather gradual. Such disorder was also evident in X-ray absorption measurements at the Zr L_3-edge, which showed a gradual increase in the effective coordination number of the Zr from near 6-coordinate in the pyrochlore rich samples to near 7-coordinate in the Tb rich defect fluorites. These results indicate the presence of ordered domains throughout the defect fluorite region, and demonstrate the gradual nature of the order−disorder transition across the $Gd_{2-x}Tb_xZr_2O_7$ series.

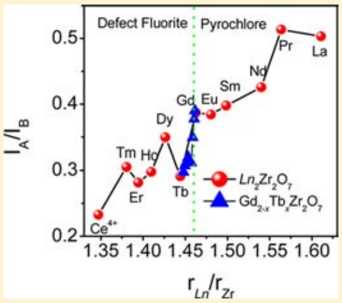

INTRODUCTION

Pyrochlore oxides of the general formula $A_2B_2O_7$ exhibit remarkable chemical and structural flexibility, resulting in a vast range of compounds with an equally vast range of applications. Depending upon composition, they exhibit a range of technologically important properties including low thermal conductivity,[1,2] high ionic conductivity,[3] and resistance to radiation[4,5] that make them suitable for use in thermal barrier coatings, solid-oxide fuel cells, and actinide immobilization, respectively. A myriad of properties is therefore possible in a single structure.

The pyrochlore structure is often described as an ordered fluorite. It belongs to space group 227 ($Fd\overline{3}m$) and contains two cation sites, 16*c* (0, 0, 0) and 16*d* (1/2, 1/2, 1/2), and three crystallographically distinct oxygen sites, 48*f* (*x*, 1/8, 1/8), 8b (3/8, 3/8, 3/8), and 8*a* (1/8, 1/8, 1/8). The 8*a* is a vacant site (Figure 1), and the *x* positional parameter of the 48*f* oxygens varies as the atoms relax toward the vacant site.[6]

A number of the useful properties exhibited by this structure appear to be related to the order−disorder phase transformation from the pyrochlore to a defect fluorite structure ($Fm\overline{3}m$), which unusually involves both the anion and cation sublattices.[6] The pyrochlore can be described as an ordered superstructure of the anion-deficient fluorite, where the order is largely driven by the size and charge difference between the cations. The order−disorder transition in lanthanoid zirconates has been extensively studied[7,8] and since the formal charge on the Ln cations remains constant across the series $Ln_2Zr_2O_7$ (Ln = Pr−Lu), the size of the A-site cations is generally considered to be the major determinant of structure.

Received: January 11, 2013
Published: July 11, 2013

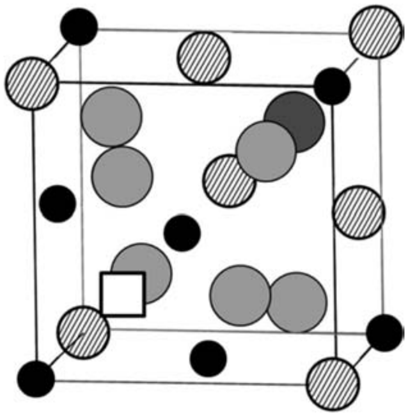

Figure 1. One-eighth of the pyrochlore unit cell illustrating the ordered A (16*d*) and B (16*c*) cation sites represented by striped and black circles, respectively. The two occupied oxygen sites, 48*f* and 8*b*, are represented by light gray and dark gray circles, respectively. The third vacant oxygen anion site, 8*a*, is represented by the square.

For the $Ln_2Zr_2O_7$ series, it is generally accepted that the pyrochlore structure is favored for lanthanoids with an ionic radius larger than Gd, and the defect fluorite structure is favored for smaller lanthanoids.[6] Yamamura et al. have investigated electrical conductivity across the $Ln_2Zr_2O_7$ series and, using X-ray diffraction (XRD), found the structures to be pyrochlore-type with Ln larger and including Gd, and fluorite-type for smaller Ln, with a corresponding electrical conductivity maximum around this boundary.[9] Generally, the size of the A-site cation can be modeled using a mixture of larger and smaller lanthanoids as illustrated in our recent study of the $Nd_{2-y}Ho_yZr_2O_7$ series.[10]

The majority of structural studies of the pyrochlore−defect fluorite transformation have used XRD as the main tool to investigate the structural transition. A small number have used neutron powder diffraction (NPD) or electron diffraction (ED), and an even smaller minority have used a combination of these with other techniques such as Raman spectroscopy. The $Nd_{2-y}Gd_yZr_2O_7$ solid solution series was examined by Mandal et al. using a combination of XRD and Raman spectroscopy. Their XRD results suggest a discontinuous pyrochlore−defect fluorite transition, but they presented evidence for local disorder in the pyrochlore phase as seen by an increase in the width of selected Raman peaks.[11] Our recent X-ray absorption near-edge spectroscopy (XANES) study on the $Ln_2Zr_2O_7$ series also showed evidence of local disorder in the pyrochlore phases that was not detected using conventional X-ray or neutron diffraction techniques.[12] Due to the nature of diffraction, and of the insensitivity of conventional powder XRD to small displacements of oxygen ions in the presence of heavy metals, it is not surprising that a technique that probes local structure such as XANES or Raman is required to provide a full description of these flexible structures.

Given the impact of disorder and the local environment on the properties of pyrochlore-type structures, the use of multiple techniques in order to achieve a complete understanding of the structure is potentially crucial in explaining observed behavior and assessing the suitability of specific compositions for use in various applications. This is particularly important for compositions near the pyrochlore−defect fluorite phase boundary. In the present work we revisit the $Gd_{2-x}Tb_xZr_2O_7$ series previously studied by Van Dijk et al.,[13] who found evidence for microdomain formation using XRD and ED. We use a combination of XRD, NPD, and XANES to investigate the disorder present across the $Gd_{2-x}Tb_xZr_2O_7$ series, and a gradual increase in disorder is revealed using neutron diffraction and X-ray absorption techniques. Comparison of the O1s XANES spectra with some well characterized Tb perovskites demonstrated the formation of tetravalent Tb in the perovskites.

■ EXPERIMENTAL SECTION

Synthesis of the $Gd_{2-x}Tb_xZr_2O_7$ ($0 \leq x \leq 2$) series. Approximately 5 g samples of each member in the series $Gd_{2-x}Tb_xZr_2O_7$ (x = 0, 0.1, 0.2, 0.3, 0.4, 0.6, 0.8, 1, 1.2, 1.4, 1.6, 1.8, and 2) were prepared using conventional solid-state methods. Before the oxides were weighed, Gd_2O_3 (Sigma-Aldrich, 99.9%), Tb_4O_7 (Sigma-Aldrich, 99.9%), and ZrO_2 (Aithaca, 99.99%) were dried overnight at 1000 °C. Stoichiometric amounts of Gd_2O_3, Tb_4O_7, and ZrO_2 were thoroughly mixed in an acetone slurry and then pressed into pellets prior to each heating step. The samples were heated in air at 1450 °C for a total of 30 days with regrinding every 3−5 days, resulting in a series with an obvious evolution of color: from off-white ($Gd_2Zr_2O_7$) to dark brown ($Tb_2Zr_2O_7$).

Synchrotron X-ray Diffraction. Data were collected on the powder diffraction beamline, 10-BM, at the Australian synchrotron[14] using a Si(111) monochromator and a MYTHEN microstrip detector. The wavelength was accurately refined to 0.82453(1) Å using LaB_6 (NIST 660a) standard. Samples were packed into 0.3 mm glass capillaries and data collected at ambient temperature in the angular range $5° < 2\theta < 80°$ in two frames shifted by 0.5° in order to cover gaps between individual detector modules. Samples were rotated during data collection to minimize the effects of preferential orientation.

Neutron Powder Diffraction. NPD for the $Tb_2Zr_2O_7$ sample was performed on the high-resolution powder diffractometer Echidna at the Open Pool Australian Lightwater (OPAL) reactor, operated by the Australian Nuclear Science and Technology Organisation (ANSTO).[15] The finely ground samples were loaded into an 8 mm vanadium can, and data were collected over the range $5° < 2\theta < 160°$ with a step size of 0.05° (2θ) with the wavelength of the incident neutrons fixed at 1.300 Å. This wavelength was obtained using a Ge (337) monochromator and calibrated against an Al_2O_3 standard.

NPD patterns for the $Gd_{2-x}Tb_xZr_2O_7$ series were collected using the D4 diffractometer at the Institut Laue-Langevin (ILL), Grenoble.[16] The sample holders had an annular geometry such that the powder was packed between the walls of two concentric cylindrical vanadium cans. The inner diameter was 8.0 mm, and the outer diameter was 10.0 mm, resulting in a thin area in which the powder was placed. Neutrons with wavelengths of λ = 0.4972 Å were obtained using a Cu(220) monochromator and rhodium filter. Data were collected over the range $5° < 2\theta < 135°$.

All diffraction data were analyzed using the Rietveld method. In the case of the neutron refinements, due to structure present in the background (caused by the sample environment), the background was estimated using a linear interpolation between a series of visually selected points. The neutron pattern peak shapes were described using a pseudo-Voigt function. Under the conditions employed, the D4 diffractometer does not have the resolution necessary for the refinement of accurate anisotropic atomic displacement parameters (ADPs), so these were refined isotropically. The peak shape in the synchrotron data was modeled using a pseudo-Voigt function, and the background was estimated using a fifth-order polynomial in 2θ.

XANES. Zr L_3-edge XANES spectra were collected on beamline 16A1 at the National Synchrotron Radiation Research Center (NSRRC) in Hsinchu, Taiwan.[17] Finely ground samples were dispersed onto Kapton tape and placed in front of the X-ray beam at a 45° angle. Spectra were collected in fluorescence yield (FLY) mode using a Lytle detector. An energy step-size of 0.2 eV was used near the absorption edge. The Zr L_3-edge spectra were calibrated against elemental Zr with the maxima in the first derivative of the L_3-edge set to 2222.3 eV.[18]

O K-edge and Tb M_5-edge XANES spectra were collected on the Soft X-ray Beamline at the Australian Synchrotron.[19] Powder samples were thinly dusted onto double-sided carbon tape (SPI Supplies) and inserted into the vacuum chamber via a load lock. The pressure inside the analysis chamber was maintained at better than $\sim 10^{-9}$ Torr. Spectra were collected from ~20 eV below to ~65 eV above the edge using X-ray fluorescence yield mode. All spectra were taken simultaneously with a total electron yield (TEY) signal measured from an Al_2O_3 (O K-edge) or Tb (Tb M_5-edge) reference foil in the beamline. The reference foil removed approximately 10% of the beam intensity. Both the O K-edge profile of Al_2O_3 and Tb M_5-edge of metallic Tb are well-known, with a distinct feature located at 531.5 and 1241.1 eV, respectively.[18,20] This allowed for a precise energy calibration of the spectra from the various samples.

All XANES spectra were analyzed using the Athena software program.[18]

RESULTS AND DISCUSSION

X-ray and Neutron Diffraction. The synchrotron X-ray diffraction (S-XRD) profile of $Gd_2Zr_2O_7$, shown in Figure 2, contains superlattice reflections indicative of the pyrochlore structure. However, consistent with the results of a recent paper,[12] there were other features in the diffraction pattern that suggest the presence of a disordered phase. The main reflections have small shoulders at lower angles, which were modeled as a fluorite-type phase. This improved the refinement dramatically and accounted for the extra intensity on these peaks. Furthermore, the main peaks also have another small very broad feature at higher angles; this will be discussed below.

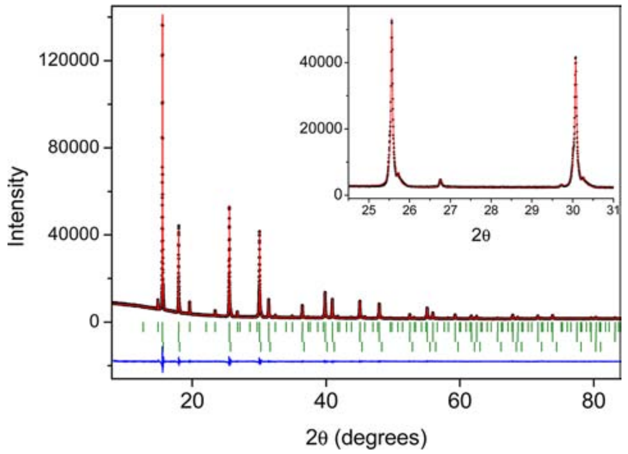

Figure 2. Synchrotron X-ray diffraction profile for $Gd_2Zr_2O_7$ obtained with $\lambda = 0.82453$ Å. The solid line is the fit to the model described in the text. The inset shows the asymmetry on the main peaks, modeled here as a cubic ZrO_2 phase. The vertical markers are due to, from top, pyrochlore, defect fluorite, and ZrO_2. The increase in intensity at low angles is due to scatter from air.

Weak pyrochlore superlattice reflections were observed in the S-XRD patterns for compositions up to and including the $Gd_{1.4}Tb_{0.6}Zr_2O_7$ sample (Figure 3a; at the scale of this figure an increase in intensity at low angles due to scatter from air is apparent). For all other compositions, only reflections indicative of a fluorite phase were observed. The data were analyzed by the Rietveld method, and the lattice parameters are shown in Figure 3b. The peaks tended to be considerably broader in the fluorite structures than in the pyrochlore phases, and asymmetry in the main peaks was present throughout the entire series. For example the fluorite (220) reflection in $Tb_2Zr_2O_7$ had a hwhm of 0.13°, whereas the corresponding peak in $Gd_2Zr_2O_7$ had a hwhm of 0.066°. The asymmetry, illustrated in the Supporting Information, is attributed to strain caused by crystallographic domain boundaries and the poorly crystalline disordered material that forms in between these.[21] This residual intensity was modeled using a second phase (a cubic fluorite), in an approach similar to that employed in other studies.[22] The synchrotron diffraction data clearly suggest an abrupt transition from samples where the pyrochlore and fluorite phases coexist, to those that only contain a defect fluorite phase beyond the $x = 0.6$ composition.

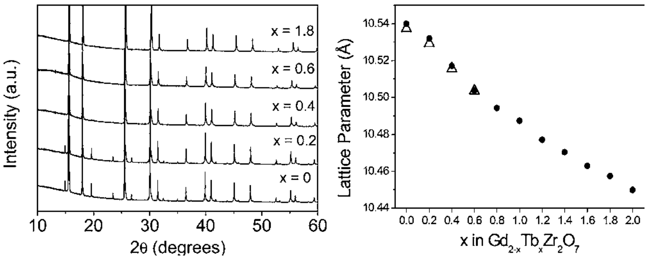

Figure 3. (left, a) Selected S-XRD patterns for members of the $Gd_{2-x}Tb_xZr_2O_7$ series (x = 0, 0.2, 0.4, 0.6, 1.8). (right, b) Lattice parameters obtained from S-XRD refinements of the $Gd_{2-x}Tb_xZr_2O_7$ series; the pyrochlore (up to $x = 0.6$) represented by the triangles has unit cell length approximately equal to twice that of the fluorite (circles). Where not apparent the ESDs are smaller than the symbols.

Neutron diffraction was also performed on selected members of the $Gd_{2-x}Tb_xZr_2O_7$ series (x = 0, 0.2, 0.4, 0.6, 1.2, 1.4, 1.6, 1.8). In order to overcome the strong absorption of thermal neutrons by gadolinium, we utilized neutrons of $\lambda \approx 0.5$ Å produced using a hot source. The peak width resolution of the diffractometer employed in this work is modest, resulting in larger than typical errors in the refined lattice parameters (and hence bond distances). To minimize this effect we fixed the lattice parameters to the values obtained from the higher resolution S-XRD measurements. In the case where the pyrochlore phase was present in NPD but not S-XRD, the pyrochlore lattice parameter was estimated by extrapolating the values obtained using Vegard's law. The data collected for the $x = 0$ and 0.2 samples had relatively poor counting statistics, and detailed analysis of these is not included here.

A representative diffraction pattern is shown in Figure 4, for the $x = 0.6$ sample. The high background in this figure is mostly due to small sample size. In the refinements against these data, the fit was significantly improved by the use of a two-phase pyrochlore plus defect fluorite model relative to that obtained when only one phase was used. For example, for $Gd_{0.8}Tb_{1.2}Zr_2O_7$, R_p improved from 1.45% for only defect fluorite to 0.90% for pyrochlore plus defect fluorite. However, the width of the pyrochlore peaks suggests that the pyrochlore phase is not completely ordered. As the S-XRD data show no evidence for cation order in samples with $x > 0.6$, we conclude that the ordering is confined to the oxygen anions.

Neutron data were collected for the Gd-free sample ($Tb_2Zr_2O_7$) using an instrument designed to give high resolution data (Echidna, ANSTO), and as discussed in a recent paper,[12] this demonstrates the absence of any pyrochlore superlattice reflections. There was, however, evidence for short-range correlations in the background, which displayed the same structured modulation seen in the defect fluorite $La_2Ce_2O_7$.[23] This appears to be a feature of the defect fluorite structure, and

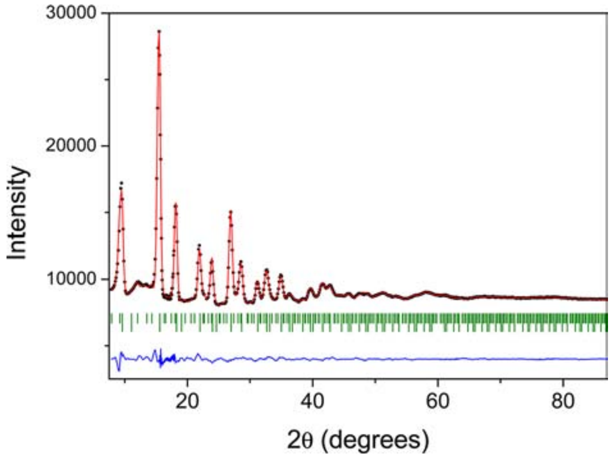

Figure 4. Neutron diffraction profile for $Gd_{1.4}Tb_{0.6}Zr_2O_7$ obtained with $\lambda \approx 0.497$ Å using the hot source. Both a pyrochlore (upper tick marks) and a defect fluorite (lower tick marks) phase were included in the refined model with $R_{wp} = 1.06\%$. The structural parameters derived from the refinement are given in Table 1.

presumably arises from local ordering of the anions and their associated vacancies. Electron diffraction patterns were obtained for selected compositions, and these contained diffuse features indicative of disorder, see Supporting Information. Further analysis of the ED is ongoing.

Rietveld analysis against the neutron diffraction data revealed the 8*a* site to be partially occupied in most samples, consistent with a slightly disordered pyrochlore phase. Occupancy of the 8*a* site requires disorder of anions from either the 48*f* or 8*b* sites. Initially, the possibility that anion occupancy on the 8*a* originates from the 48*f* site was tested, this being identified by Grimes and co-workers as the most likely occurrence.[24] In this case the total ($n8a + n48f$) occupancy was constrained to maintain charge neutrality. In doing so we have neglected the presence of the small amount of Tb^{4+} detected in the spectroscopic analysis (see below) since it was not possible to precisely estimate this. Refinement using such a constraint resulted in negative occupancy of the 8*a* site, suggesting that the 48*f* site was fully occupied. Consequently, the possibility that the anions were disordered over the 8*a* and 8*b* sites was tested, and such models gave stable refinements. In these refinements, the atomic displacement parameter (ADP) values in the 8*a* and 8*b* sites were constrained to be equal.

We observe a small increase in the occupancy of the 8*a* site (and corresponding decrease in 8*b* occupancy) with the increase of Tb content. This result is surprising; it had been expected that the occupancy of the normally vacant site would originate from the site with a greater amount of anions (the 48*f* site); indeed, previous studies have shown this to be the case.[25,26] This may reflect the importance of the Zr_2O_6 framework on the stability of the pyrochlore structure, or it may be a consequence of the disorder of the cations.[24] The statistical limits of the refinement process preclude detailed interpretation of this observation, and further investigations are needed to determine the extent to which disorder from the 8*b* site is contributing to the 8*a* site occupancy.

The defect fluorite structure has one-eighth of the anion sites vacant, corresponding to an oxygen occupancy of 88%. Using the 7/8 occupancy in the refinement of most of the samples resulted in unreasonably large ADPs for the anion sites, suggesting that the site occupancy was less. When the fluorite-type oxygen occupancy was refined, it decreased to around 80%, which decreased the ADPs to more physically reasonable values (Table 1). This is evidence that the total Tb^{4+} present in the samples is small, since large amounts of this would increase the oxygen occupancy. That the refined occupancy of the anion sites is less than expected is possibly related to the diffuse background evident in the neutron profiles, and is consistent with the use of pyrochlores as fast-ion conductors.

In summary, while S-XRD data suggest a transition from the coexistence of pyrochlore and defect fluorite phases to a single defect fluorite phase, the neutron data not only provide evidence for independent ordering of the anion and cation sublattices but also suggest that the disorder transition across the pyrochlore−defect fluorite boundary of $Gd_{2-x}Tb_xZr_2O_7$ is rather gradual.

Zr L_3-Edge XANES. Zr L_3-edge XANES spectra were collected for several compounds in the $Gd_{2-x}Tb_xZr_2O_7$ series (Figure 5a). The L_3-edge corresponds to the dipole-allowed transition of a $2p_{3/2}$ electron into unoccupied 4*d* states. As demonstrated in our previous study of lanthanide zirconates $Ln_2Zr_2O_7$,[12] the line shape is dependent on the coordination number (CN) of Zr. The effective coordination number of the

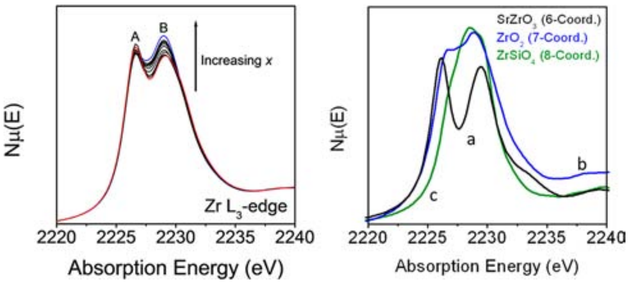

Figure 5. (left, a) Zr L_3-edge XANES spectra of $Gd_{2-x}Tb_xZr_2O_7$. (right, b) Zr L_3-edge XANES spectra of the 6, 7, and 8 coordinate standards, labeled a, b, and c, respectively. All spectra were collected in fluorescence mode.

Table 1. Atomic Positions, Isotropic Atomic Displacement Parameters, and Site Occupancies for $Gd_{1.4}Tb_{0.6}Zr_2O_7$ Refined against Neutron Diffraction Data Using a Two-Phase Model

space group	*a* (Å)	R_{wp}	R_P	wt % of phase	atom	site	*x*	*y*	*z*	B_{iso} (Å)^2	occ
$Fd\bar{3}m$	10.5036	1.06	0.64	19	Gd/Tb	16*d*	1/2	1/2	1/2	0.9(2)	1
					Zr	16*c*	0	0	0	0.8(2)	1
					O (1)	48*f*	0.334(2)	1/8	1/8	1.6(3)	1
					O (2)	8*b*	3/8	3/8	3/8	0.4(3)	0.73(7)
					O (3)	8*a*	1/8	1/8	1/8	1(2)	0.27(7)
$Fm\bar{3}m$	5.2518	1.06	0.64	81	Gd/Tb/Zr	4*a*	0	0	0	1.9(3)	1
					O	8*c*	1/4	1/4	1/4	3.6(2)	0.782(1)

Zr increases from 6 in pyrochlore to 7 in defect fluorite. In general, two features (labeled A and B) are observed in all Zr L_3-edge XANES spectra. Figure 5b displays the line-shape variation between the measured standards with Zr^{4+} in 6, 7, and 8 coordinate environments. Typically, features A and B correspond to the t_{2g} and e_g states under octahedral symmetry, respectively, and the energy difference between these features is proportional to the crystal-field splitting.[12,27]

To extract quantitative information on the Zr coordination environment, the Zr L_3-edge XANES spectra were fitted to component peaks. As shown in Figure 6a, the Zr L_3-edge XANES spectra were fitted to 3 Gaussian-shaped peaks and a single arc-tan background to mimic the edge jump at the absorption edge.[28] Although feature A could be fitted to a single peak, two peaks (labeled B1 and B2) were required to fit feature B. In 6-coordinate octahedral systems, the e_g states are more sensitive to distortions of the local structure due to the overlap of d_{z^2} and $d_{x^2-y^2}$ states with ligand states,[29] resulting in peak broadening and splitting. Similar broadening was also observed in $Ln_2Zr_2O_7$ and $Pb(Zr_{1-x}Ti_x)O_3$.[12,30] The intensity of peak B2 decreases relative to that of B1 across the series, which may indicate increased disorder across the series.[30]

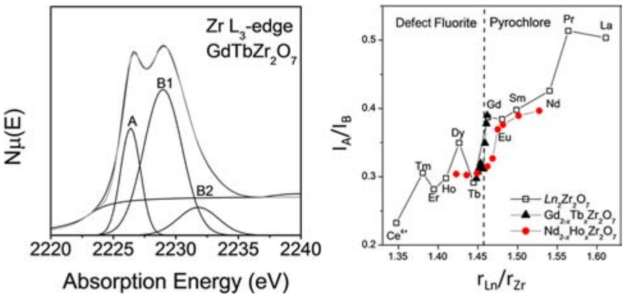

Figure 6. (left, a) Fitted Zr L_3-edge XANES spectrum of $GdTbZr_2O_7$. (right, b) Plots of the radius ratio r_{Ln}/r_{Zr} as a function of the intensity ratio of features A and B (I_A/I_B, where $I_B = I_{B1} + I_{B2}$). Dashed line represents the pyrochlore−defect fluorite phase boundary.

Overall, the $Gd_{2-x}Tb_xZr_2O_7$ series follows the same trends that were observed in the parent rare-earth zirconates $Ln_2Zr_2O_7$. When plotted as a function of the radius ratio of the Ln and Zr atoms (r_{Ln}/r_{Zr}), the intensity ratio of features A and B (I_A/I_B) decreases as r_{Ln}/r_{Zr} decreases (Figure 6b), indicating an increase in the Zr CN. A corresponding decrease in crystal-field splitting (ΔE) was expected to occur as the CN of Zr increases.[27] However, it was observed that ΔE was essentially independent of cation size across the $Gd_{2-x}Tb_xZr_2O_7$ series (Figure 5a). This is likely due to the small difference in the ionic radii of Gd (1.053 Å) and Tb (1.04 Å).[31] The expected decrease in ΔE, as well as I_A/I_B, was observed for the $Nd_{2-x}Ho_xZr_2O_7$ series in the pyrochlore region (Figure 6b), where there is a much larger difference in the size of the Nd (1.109 Å) and Ho (1.015 Å) atoms.[31] However, there is little to no change in both ΔE and I_A/I_B once the $Nd_{2-x}Ho_xZr_2O_7$ series forms a fully disordered structure, suggesting that there are no further decreases in the CN of Zr. Surprisingly, I_A/I_B changes in a near linear fashion across the entire $Gd_{2-x}Tb_xZr_2O_7$ series, even after the defect fluorite structure has formed. The observation of continuous disorder across the pyrochlore−defect fluorite phase boundary can be explained by the existence of ordered regions within the defect fluorite structures; these are referred to as ordered domains.

O K-Edge XANES Spectra. Representative O K-edge XANES spectra are shown in Figure 7a, where three main features (labeled A−C) are apparent. Peaks A and B are observed in all $Gd_{2-x}Tb_xZr_2O_7$ samples and are common features in many zirconium and lanthanide oxides.[32−36] These peaks can be assigned as the transition of an O 1s electron into hybridized O 2p/Zr 4d states.[34] Peak-splitting likely occurs because of crystal-field splitting of the Zr 4d states;[34] however, this energy difference is greater than that observed in the Zr L_3-edge. Such a difference in crystal field splitting was also observed in $Gd_2Ti_2O_7$ where it was attributed to a greater sensitivity of the Ti L-edge to distortions of the Ti coordination environment and the contributions of Gd^{3+} states near the absorption edge.[33] It is likely that similar factors may also affect the crystal-field splitting in the zirconate pyrochlores. A small decrease in the intensity of peak A, relative to peak B, is observed across the series. While the change in intensity is small (it is most noticeable by comparison of spectra from the two end members $Gd_2Zr_2O_7$ and $Tb_2Zr_2O_7$), it is consistent with the changes observed in the Zr L_3-edge XANES spectra.

Although there are few differences in peaks A and B across the series, a third peak (labeled C) forms below the absorption edge as x, and hence the amount of defect fluorite increases. This is absent in $Gd_2Zr_2O_7$ and evidently due to the presence of Tb. A similar peak is typically observed in tetravalent lanthanide oxides and can be assigned as an O 1s to O 2p/Ln 4f transition.[35−37] In the absence of a well characterized Tb^{+4} pyrochlore sample we utilized some Tb containing perovskites as standards in our XANES analysis. A peak near 529.5 eV is

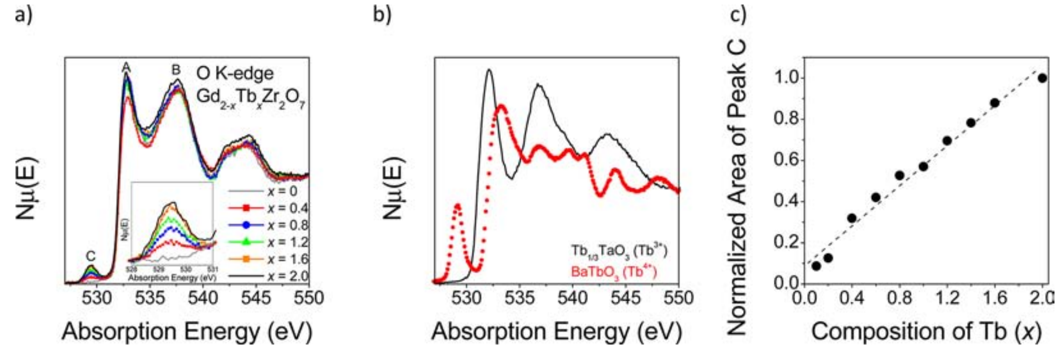

Figure 7. (a) O K-edge XANES spectra of $Gd_{2-x}Tb_xZr_2O_7$ (where x = 0, 0.4, 0.8, 1.2, 1.6, 2). The inset shows the change in the intensity of peak C across the $Gd_{2-x}Tb_xZr_2O_7$ series. (b) The O K-edge XANES spectra of $Tb_{1/3}TaO_3$ (Tb^{3+}) and $BaTbO_3$ (Tb^{4+}). (c) Plot of the area of feature C, normalized to the peak area of $Tb_2Zr_2O_7$, with respect to the composition of Tb (x). All spectra were collected in fluorescence mode.

clearly visible in tetravalent $BaTbO_3$ but absent in trivalent $Tb_{1/3}TaO_3$ (Figure 7b). This transition occurs at higher absorption energy (possibly near feature B) in trivalent lanthanides (shift to higher absorption energy is consistent with greater screening of the $4f^n$ ground state versus the $4f^{n-1}$ ground state). As this peak is dependent upon x, it is likely that a small amount of Tb^{4+} forms in these compounds, consistent with the increase of dark brown color across the series, which is most likely related to the existence of Tb^{3+}/Tb^{4+}. There is a general decrease in the intensity of feature A with decreasing x (Figure 7a), which is consistent with a decrease in tetravalent Tb as the composition of Tb decreases. Additional evidence of mixed-valent Tb^{3+}/Tb^{4+} can be found in the Tb M_5-edge XANES which corresponds to the transition of $3d_{5/2}$ electron into empty 4f states. The final state of Tb^{3+} is significantly different from that of Tb^{4+}. As shown in Figure 8a, the line shape of $Tb_{1/3}TaO_3$ has three main features that are distinctly different from the two main features of $BaTbO_3$. These features are commonly used to identify the presence of Tb^{3+} and Tb^{4+}.[38,39] When comparing the Tb M_5-edge XANES spectra of $Tb_2Sn_2O_7$, a pyrochlore containing only Tb^{3+},[40] $Tb_2Zr_2O_7$ shows broadening toward higher absorption energy that is consistent with the presence of a small amount of Tb^{4+} (Figure 8b). Similar evidence of Tb^{4+} was also observed in the Tb 4d XPS spectra (see the Supporting Information). This suggests partial occupancy of the O vacancies in the defect fluorite phases, although this may be too small to be detected using neutron diffraction.

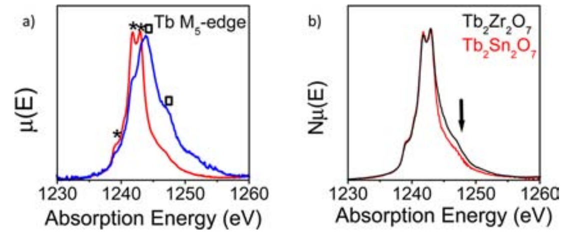

Figure 8. (a) Tb M_5-edge XANES spectra of $Tb_{1/3}TaO_3$ (red) and $BaTbO_3$ (blue). Characteristic features of Tb^{3+} and Tb^{4+} are labeled as * and □, respectively. (b) Tb M_5-edge of $Tb_2Sn_2O_7$ (red) and $Tb_2Zr_2O_7$ (black). All XANES spectra were collected in TEY mode.

It is important to note that although the mixed valent Tb_4O_7 was used in the synthesis, Tb has been shown to be readily reduced at high temperatures in pyrochlores.[39] In general the oxidation state of the Tb is determined by a combination of the lattice and preparation conditions, for example the perovskites $BaTbO_3$ and $Tb_{1/3}TaO_3$ contain Tb^{4+} and Tb^{3+} respectively, yet both are prepared from reaction of Tb_4O_7 in air.[41] The related pyrochlore $Tb_2Sn_2O_7$, formed by heating Tb_4O_7 and SnO_2 prepared in air, contained only Tb^{3+}. The O K-line shows that the amount of Tb^{4+} increased as the defect fluorite content increased across the $Gd_{2-x}Tb_xZr_2O_7$ series. The formation of Tb^{4+} might be related to the local geometry of the Tb cations in the defect fluorite phase. It appears that the compressed scalenohedral coordination of the Tb in the pyrochlore structure favors Tb^{3+} whereas the approximate cubic environment in the defect fluorite favors Tb^{4+}. Unfortunately the Tb M_5-edge is not sufficiently sensitive to the geometry to allow us to verify this.

■ CONCLUSION

In order to investigate the nature of the pyrochlore−defect fluorite order−disorder transition across the $Ln_2Zr_2O_7$ series, which occurs between Ln = Gd and Ln = Tb, a series of oxides of the type $Gd_{2-x}Tb_xZr_2O_7$ were prepared and characterized using a combination of diffraction and spectroscopy techniques. Synchrotron XRD data show that at low Tb contents the samples are predominantly pyrochlore-type, although small amounts of fluorite-type phase are also present for $x \leq 0.6$. Increasing the amount of the smaller Tb cation results in a discontinuous transition to single phase defect fluorite structures for compositions with $x > 0.6$ ($Gd_{1.4}Tb_{0.6}Zr_2O_7$). In order to minimize the absorption in the Gd-containing samples, neutron diffraction data were collected using short wavelength neutrons (λ = 0.4972 Å). Such data provided evidence for partial oxygen anion order for $x > 0.6$. XANES was employed to analyze the Zr L_3-edge, revealing a gradual increase in the coordination number of Zr^{4+} with increasing Tb content, presumably from a near 6-coordinate environment in the regular pyrochlore to an effective 7-coordinate environment in the defect fluorite. These results indicate the presence of ordered domains throughout the defect fluorite region and show the gradual nature of the disorder transition across the $Gd_{2-x}Tb_xZr_2O_7$ series. O K-edge XANES spectra provide evidence for the presence of a small amount of Tb^{4+} in the samples, which was confirmed by measurement of the Tb M_5 XANES and Tb 4*d* XPS spectra.

■ ASSOCIATED CONTENT

Ⓢ Supporting Information

Additional experimental details as discussed in the text. This material is available free of charge via the Internet at http://pubs.acs.org.

■ AUTHOR INFORMATION

Corresponding Author

* E-mail: b.kennedy@chem.usyd.edu.au.

Notes

The authors declare no competing financial interest.

■ ACKNOWLEDGMENTS

This work was, in part, performed at the powder diffraction beamline with the assistance of Dr. Helen Brand, as well as the Soft X-ray Spectroscopy beamline with the assistance of Dr. Bruce Cowie at the Australian Synchrotron. We thank Drs. Mark Blackford and Greg Lumpkin from ANSTO for measurement of electron diffraction patterns. The work performed at the NSRRC was supported by the Australian Synchrotron International Access Program. We acknowledge the Australian Research Council and AINSE for financial support.

■ REFERENCES

(1) Lehmann, H.; Pitzer, D.; Pracht, G.; Vassen, R.; Stöver, D. *J. Am. Ceram. Soc.* **2003**, *86*, 1338.

(2) Wu, J.; Wei, X. Z.; Padture, N. P.; Klemens, P. G.; Gell, M.; Garcia, E.; Miranzo, P.; Osendi, M. I. *J. Am. Ceram. Soc.* **2002**, *85*, 3031.

(3) Tuller, H. L. *Solid State Ionics* **1992**, *52*, 135.

(4) Weber, W. J.; Ewing, R. C.; Catlow, C. R. A.; de la Rubia, T. D.; Hobbs, L. W.; Kinoshita, C.; Matzke, H.; Motta, A. T.; Nastasi, M.; Salje, E. K. H.; Vance, E. R.; Zinkle, S. J. *J. Mater. Res.* **1998**, *13*, 1434.

(5) Lian, J.; Helean, K. B.; Kennedy, B. J.; Wang, L. M.; Navrotsky, A.; Ewing, R. C. *J. Phys. Chem. B* **2006**, *110*, 2343.

(6) Subramanian, M. A.; Aravamudan, G.; Subba Rao, G. V. *Prog. Solid State Chem.* **1983**, *15*, 55.

(7) Kutty, K. V. G.; Mathews, C. K.; Rao, T. N.; Varadaraju, U. V. *Solid State Ionics* **1995**, *80*, 99.

(8) Uno, M.; Kosuga, A.; Okui, M.; Horisaka, K.; Muta, H.; Kurosaki, K.; Yamanaka, S. *J. Alloys Compd.* **2006**, *420*, 291.

(9) Yamamura, H.; Nishino, H.; Kakinuma, K.; Nomura, K. *Solid State Ionics* **2003**, *158*, 359.

(10) Clements, R.; Hester, J. R.; Kennedy, B. J.; Ling, C. D.; Stampfl, A. P. J. *J. Solid State Chem.* **2011**, *184*, 2108.

(11) Mandal, B. P.; Banerji, A.; Sathe, V.; Deb, S. K.; Tyagi, A. K. *J. Solid State Chem.* **2007**, *180*, 2643.

(12) Blanchard, P. E. R.; Clements, R.; Kennedy, B. J.; Ling, C. D.; Reynolds, E.; Avdeev, M.; Stampfl, A. P. J.; Zhang, Z.; Jang, L.-Y. *Inorg. Chem.* **2012**, *51*, 13237.

(13) Van Dijk, M. P.; de Vries, K. J.; Burggraaf, A. J. *Solid State Ionics* **1983**, *9 &10*, 913.

(14) Wallwork, K. S.; Kennedy, B. J.; Wang, D. *AIP Conf. Proc.* **2007**, *879*, 879.

(15) Liss, K.-D.; Hunter, B.; Hagen, M.; Noakes, T.; Kennedy, S. *Phys. B (Amsterdam, Neth.)* **2006**, *385−86*, 1010.

(16) Fischer, H. E.; Cuello, G. J.; Palleau, P.; Feltin, D.; Barnes, A. C.; Badyal, Y. S.; Simonson, J. M. *Appl. Phys. A: Mater. Sci. Process.* **2002**, *74*, 160.

(17) Dann, T. E.; Chung, S. C.; Huang, L. J.; Juang, J. M.; Chen, C. I.; Tsang, K. L. *J. Synchrotron Radiat.* **1998**, *5*, 664.

(18) Ravel, B.; Newville, M. *J. Synchrotron Radiat.* **2005**, *12*, 537.

(19) Cowie, B. C. C.; Tadich, A.; Thomsen, L. *AIP Conf. Proc.* **2010**, *1234*, 307.

(20) Henderson, G. S.; Neuville, D. R.; Cormier, L. *Chem. Geol.* **2009**, *259*, 54.

(21) Daniels, J. E.; Jones, J. L.; Finlayson, T. R. *J. Phys. D: Appl. Phys.* **2006**, *39*, 5294.

(22) Theissmann, R.; Ehrenberg, H.; Weitzel, H.; Fuess, H. *J. Mater. Sci.* **2002**, *37*, 4431.

(23) Reynolds, E.; Blanchard, P. E. R.; Zhou, Q. D.; Kennedy, B. J.; Zhang, Z. M.; Jang, L. Y. *Phys. Rev. B* **2012**, *85*, 132101.

(24) Pirzada, M.; Grimes, R. W.; Minervini, L.; Maguire, J. F.; Sickafus, K. E. *Solid State Ionics* **2001**, *140*, 201.

(25) Whittle, K. R.; Cranswick, L. M. D.; Redfern, S. A. T.; Swainson, I. P.; Lumpkin, G. R. *J. Solid State Chem.* **2009**, *182*, 442.

(26) Heremans, C.; Wuensch, B. J.; Stalick, J. K.; Prince, E. *J. Solid State Chem.* **1995**, *117*, 108.

(27) Galoisy, L.; Pelegrin, E.; Arrio, M. A.; Ildefonse, P.; Calas, G. *J. Am. Ceram. Soc.* **1999**, *82*, 2219.

(28) Zhang, F.; Chupas, P. J.; Lui, S. L. A.; Hanson, J. C.; Caliebe, W. A.; Lee, P. L.; Chan, S. W. *Chem. Mater.* **2007**, *19*, 3118.

(29) Schneller, T.; Kohlstedt, H.; Petraru, A.; Waser, R.; Guo, J.; Denlinger, J.; Learmonth, T.; Glans, P. A.; Smith, K. E. *J. Sol-Gel Sci. Technol.* **2008**, *48*, 239.

(30) Henderson, G. S.; Liu, X.; Fleet, M. E. *Phys. Chem. Miner.* **2002**, *29*, 32.

(31) Shannon, R. D. *Acta Crystallogr., Sect. A* **1976**, *32*, 751.

(32) Nachimuthu, P.; Thevuthasan, S.; Adams, E. M.; Weber, W. J.; Begg, B. D.; Mun, B. S.; Shuh, D. K.; Lindle, D. W.; Gullikson, E. M.; Perera, R. C. C. *J. Phys. Chem. B* **2005**, *109*, 1337.

(33) Nachimuthu, P.; Thevuthasan, S.; Engelhard, M. H.; Weber, W. J.; Shuh, D. K.; Hamdan, N. M.; Mun, B. S.; Adams, E. M.; McCready, D. E.; Shutthanandan, V.; Lindle, D. W.; Balakrishnan, G.; Paul, D. M.; Gullikson, E. M.; Perera, R. C. C.; Lian, J.; Wang, L. M.; Ewing, R. C. *Phys. Rev. B* **2004**, *70*, 100101.

(34) Lee, Y. H.; Chen, J. M.; Lee, J. F.; Kao, H. C. I. *J. Chin. Chem. Soc.* **2009**, *56*, 543.

(35) Wang, X. Q.; Hanson, J. C.; Liu, G.; Rodriguez, J. A.; Iglesias-Juez, A.; Fernandez-Garcia, M. *J. Chem. Phys.* **2004**, *121*, 5434.

(36) Wang, X. Q.; Hanson, J. C.; Rodriguez, J. A.; Belver, C.; Fernandez-Garcia, M. *J. Chem. Phys.* **2005**, *122*, 154711.

(37) Mullins, D. R.; Overbury, S. H.; Huntley, D. R. *Surf. Sci.* **1998**, *409*, 307.

(38) Vanderlaan, G.; Fuggle, J. C.; Vandijk, M. P.; Burggraaf, A. J.; Esteva, J. M.; Karnatak, R. *J. Phys. Chem. Solids* **1986**, *47*, 413.

(39) Hu, Z. W.; Kaindl, G.; Muller, B. G. *J. Alloys Compd.* **1997**, *246*, 177.

(40) Kennedy, B. J.; Hunter, B. A.; Howard, C. J. *J. Solid State Chem.* **1997**, *130*, 58.

(41) Zhou, Q. D.; Saines, P. J.; Sharma, N.; Ting, J.; Kennedy, B. J.; Zhang, Z. M.; Withers, R. L.; Wallwork, K. S. *Chem. Mater.* **2008**, *20*, 6666.